Automated classification of heat sources detected using SWIR remote sensing

Soushi Kato [a,*], Hiroki Miyamoto [b], Stefania Amici [c], Atsushi Oda [a], Hiroyuki Matsushita [a], Ryosuke Nakamura [a]

[a] National Institute of Advanced Industrial Science and Technology, 2-4-7 Aomi, Koto, Tokyo 135-0064, Japan
[b] First Loop Technologies, 2-13-10 Okubo, Shinjuku, Tokyo 169-0072, Japan
[c] Istituto Nazionale di Geofisica e Vulcanologia, Via di Vigna Murata 605, 00143 Rome, Italy

ARTICLE INFO

ABSTRACT

The potential of shortwave infrared (SWIR) remote sensing to detect hotspots has been investigated using satellite data for decades. The hotspots detected by satellite SWIR sensors include very high-temperature heat sources such as wildfires, volcanoes, industrial activity, or open burning. This study proposes an automated classification method of heat source detected utilizing Landsat 8 and Sentinel-2 data. We created training data of heat sources via visual inspection of hotspots detected by Landsat 8. A scheme to classify heat sources for daytime data was developed by combining classification methods based on a Convolutional Neural Network (CNN) algorithm utilizing spatial features and a decision tree algorithm based on thematic land-cover information and our time series detection record. Validation work using 10,959 classification results corresponding to hotspots acquired from May 2017 to July 2019 indicated that the two classification results were in 79.7% agreement. For hotspots where the two classification schemes agreed, the classification was 97.9% accurate. Even when the results of the two classification schemes conflicted, either was correct in 73% of the samples. To improve the accuracy, the heat source category was re-allocated to the most probable category corresponding to the combination of the results from the two methods. Integrating the two approaches achieved an overall accuracy of 92.8%. In contrast, the overall accuracy for heat source classification during nighttime reached 79.3% because only the decision tree-based classification was applicable to limited available data. Comparison with the Visible Infrared Imaging Radiometer Suite (VIIRS) fire product revealed that, despite the limited data acquisition frequency of Landsat 8, regional tendencies in hotspot occurrence were qualitatively appropriate for an annual period on a global scale.

1. Introduction

Biomass burning and volcanic activity have been primary targets of satellite remote sensing, which is advantageous for repetitive global coverage (Flasse and Ceccato, 1996; Leblon, 2001; Wooster et al., 2005; Lorenz, 2013). Disasters evoked by such phenomena have great impact, or inflict damages, on Earth environment and human habitats. Detecting these disasters at early stage is crucial to mitigate damages. For another example of increasing importance of monitoring hot targets, recent studies reported that climate change increases the occurrence of wildfires (Goss et al., 2020; Halofsky et al., 2020; Mueller et al., 2020; Williams et al., 2019). Although there is no evidence that shows increase of volcanic activity, 68 volcanoes had erupted during 2020 (Global

Volcanism Program, 2013).

Middle infrared (MIR, 3.0–5.0 μm) region, which is widely used to detect and monitor wildfires, is sensitive to the range of very high temperature of about 600 to 1200 K corresponding to smoldering and flaming fire (Wooster et al., 2013). For nearly two decades, the National Aeronautics and Space Administration (NASA) has been providing active fire and thermal anomaly data derived from MIR and thermal infrared (TIR, 8.0–15.0 μm) data obtained by the Moderate Resolution Imaging Spectroradiometer (MODIS), modifying the methods previously proposed for Advanced Very High Resolution Radiometer (AVHRR) data (Lee and Tag, 1990; Boles and Verbyla, 2000). Several revisions have been made for the MODIS fire algorithm to improve accuracy in detection and Fire Radiative Power (FRP) estimation based on various
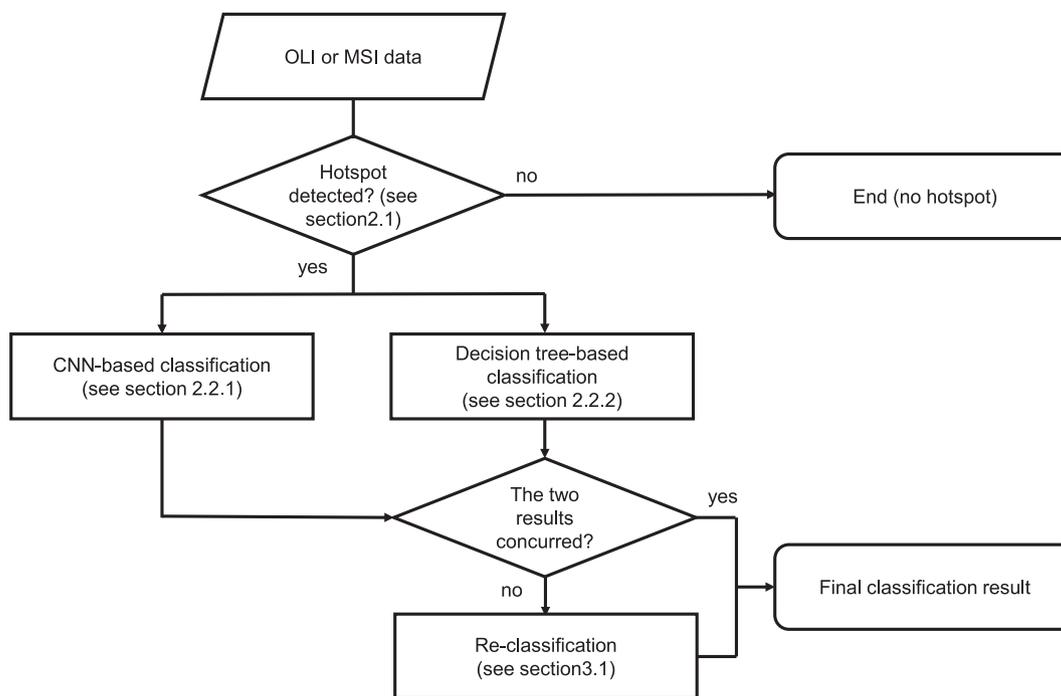
Fig. 1. Flowchart of the hotspot detection and classification of heat source category for daytime data.

validation works (Kaufman et al., 1998; Justice et al., 2002; Giglio et al., 2003; Morisette et al., 2005; Giglio et al., 2006; Giglio et al., 2008, Giglio et al., 2016). Wright et al. (2002), Wright et al., (2004), and Wright (2016) also used MODIS data to develop the MODVOLC algorithm which is focused on monitoring volcanoes worldwide. Building on the MODIS fire algorithm, Schroeder et al. (2014) and Zhang et al. (2017) proposed active fire detection algorithms for Visible Infrared Imaging Radiometer Suite (VIIRS) data which have an advantage of 375 m spatial resolution in comparison with 1 km for MODIS. These sensors are efficient at detecting active fires because of their wide swath widths (2330 km for MODIS, 3040 km for VIIRS), which enable to cover the entire Earth twice a day. The Sea and Land Surface Temperature Radiometer (SLSTR) onboard Sentinel-3A and 3B has also been used to detect active fire by using MIR band (Xu et al., 2020). Although much high frequency (15 min) of geostationary Spinning Enhanced Visible and InfraRed Imager (SEVIRI) is suitable to monitor active fires (Roberts and Wooster, 2008), estimation of fire radiative energy is the principal purpose due to coarser spatial resolution (3 km). The coarse spatial resolutions of these satellite sensors mean they are unable to indicate exact locations of heat sources, which are often subpixel-sized. The minimum of detection limit depends on the temperature and fractional area in a pixel because the detection algorithms are composed of several threshold tests for a pixel's radiance and a signal difference compared to background pixels. For example, a coarse MIR sensor (e.g., 1 km resolution) cannot detect very hot but small hotspots like small campfire or warm and large hotspots such as a geothermal area with sub-boiling hot spring when the radiance from the heat source is smaller than variation in background radiance. On the other hand, 370 m of spatial resolution allowed MIR sensor of Bi-spectral Infra-Red Detection (BIRD) to detect even 2×2 m^2 of bonfire (Lorenz, 2013). Recently, TIR bolometer cameras with a spatial resolution of about 200 m have been launched onboard satellites such as the Advanced Land Observing Satellite-2 Compact InfraRed Camera (ALOS-2 CIRC) and the University International Formation Mission (UNI-FORM), primarily to monitor wildfires (Fukuhara et al., 2017; Naitoh et al., 2013). Silvestri et al. (2020) demonstrated potential of multi-spectral TIR data observed by the ECOsystem Spaceborne Thermal Radiometer Experiment on Space Station (ECOSTRESS) to monitor volcanic activities. However, the TIR data tend to saturate over very hot targets because TIR sensors are mainly designed to resolve differences in normal surface temperature. During daytime, terrain conditions (sunlit and shaded slopes) and thermal properties (affected by reflectance, heat capacity, and evapotranspiration) drastically increase variation in surface temperature and thereby make it difficult to detect small hotspots. As Giglio et al. (2008) simulated, shortwave infrared (SWIR, 1.1–3.0 µm) region has sensitivity to hot targets of about 600 to 1000 K comparable to or better than TIR region. SWIR sensors with higher spatial resolution (~30 m) are more effective for detecting thermal anomalies, which we intend as very hot heat sources corresponding to temperature greater than about 500 K in this study. Morisette et al. (2005) used Advanced Spaceborne Thermal Emission and Reflection radiometer (ASTER) data to validate the MODIS fire products leveraging the coincident data acquisition because they are onboard the same satellite, Terra. To avoid time-consuming manual detection of fire pixels, Giglio et al. (2008) proposed the automated fire detection by using the near infrared (NIR, 0.7–1.1 µm) and SWIR bands of the ASTER. However, the ASTER data had not been employed to a continuous operation of hotspot detection because the data acquisition rate is limited to about 600 scenes (2160000 km^2) par day due to various hardware, power, and data storage, and download rate constraints (Yamaguchi et al., 1998). For Landsat 8 Operational Land Imager (OLI) launched on 2013 to continuously observe the land surface at 16 days revisit cycle, Schroeder et al. (2016) proposed a scheme to detect hotspots by using the NIR and SWIR bands. To improve omission error rate, Murphy et al. (2016), Kumar and Roy (2018) used additional SWIR band (1.6 µm) with 0.86 µm and 2.2 µm bands of OLI for hotspot detection. However, these SWIR fire detection procedures can be affected by false detections (commission error) due to highly reflective surface material, i.e., large rooftops, which can generate in the SWIR region a high spectral radiance signal that can be confused with a pixel containing fire. To detect only short-lived biomass burning, Schroeder et al. (2016) and Kumar and Roy (2018) eliminated temporally persistent heat sources, such as factories, by validating the multitemporal co-occurrence. Therefore, the detected hotspots need to be differentiated between the different categories of heat sources such as fires, volcanic eruptions, industrial activities, or false detections, unless focusing on a specific target area such as peatland fire over tropical area (Sofan et al., 2019), selected volcanoes

Table 1

Specifications of spectral bands of Landsat 8 OLI and Thermal Infrared Sensor (TIRS) and Sentinel-2 MSI.

Landsat 8 OLI and TIRS			Sentinel-2 MSI			
Band	Central wavelength (μm)	Spatial resolution (m)	Band	Central wavelength (μm)	Spatial resolution (m)	Name
1	0.443	30	1	0.443	60	Coastal aerosol
2	0.482	30	2	0.490	10	Blue
3	0.561	30	3	0.560	10	Green
4	0.655	30	4	0.665	10	Red
8	0.590	15				PAN
			5	0.705	20	Red-edge 1
			6	0.740	20	Red-edge 2
			7	0.783	20	Red-edge 3
			8	0.842	10	NIR wide
5	0.865	30	8A	0.865	20	NIR narrow
			9	0.945	60	Water vapor
9	1.373	30	10	1.375	60	Cirrus
6	1.609	30	11	1.610	20	SWIR 1
7	2.201	30	12	2.190	20	SWIR 2
10	10.9	100				Thermal 1 (TIRS)
11	12.0	100				Thermal 2 (TIRS)

(Marchese et al., 2019), or vegetation areas (Hu et al., 2021). We propose method for automatic identification of high-temperature sources, which can be easily adapted to new generation of satellites.

In addition to existing global monitoring fires systems such as the Fire Information for Resource Management System (FIRMS) managed by NASA (Davies et al., 2009), hotspot detection can be possibly implemented by using NIR and SWIR data in fact of the Copernicus multispectral Sentinel-2 constellation satellites can observe (in cloud-free condition) the same area every 5 days in wavebands comparable with Landsat 8 OLI. Recent open and free policies regarding Earth observation satellite data enable any user to access huge amount of data on a global scale. An extensive data processing ranging between Landsat 8 OLI from 2013 to present and Sentinel-2 MSI from 2018 to present has been implemented to develop and validate the new hotspot detection system based on SWIR bands. Utilizing the hotspots detected during the period studied as training data, we constructed a scheme to automatically classify hotspots according to heat source categories. Two independent classification methods have been developed in this study: 1) is based on Convolutional Neural Network (CNN) algorithm and 2) is based on an empirical decision tree algorithm. Accuracies corresponding to these two classification methods were assessed for each classification category. An additional re-classification of the result which uses a combination of the two classification results was developed to improve the accuracy of the classification.

2. Methods

The proposed method is composed of two parts, namely hotspot detection described in Section 2.1 and heat source classification, for which we developed two different methods described in Section 2.2. The hotspots detected in daytime undergo an additional re-classification based on the combination of the two classification results. The re-classification scheme is described in Section 3.1 instead of this section because the classification rules were established based on the validation results of the individual classification methods. The outline of our algorithm is depicted in Fig. 1.

2.1. Hotspot detection

To define heat source categories and to develop algorithms to classify them, the amount and quality of the training data are essential. Therefore, the hotspot dataset was generated in advance of developing our heat source classification methods. Starting from the thresholding equation developed by Giglio et al. (2008) to detect hotspots, we have retrieved empirical thresholds to be used on Landsat 8 OLI and Sentinel-2 MSI data, whose spectral bands are summarized in Table 1. To
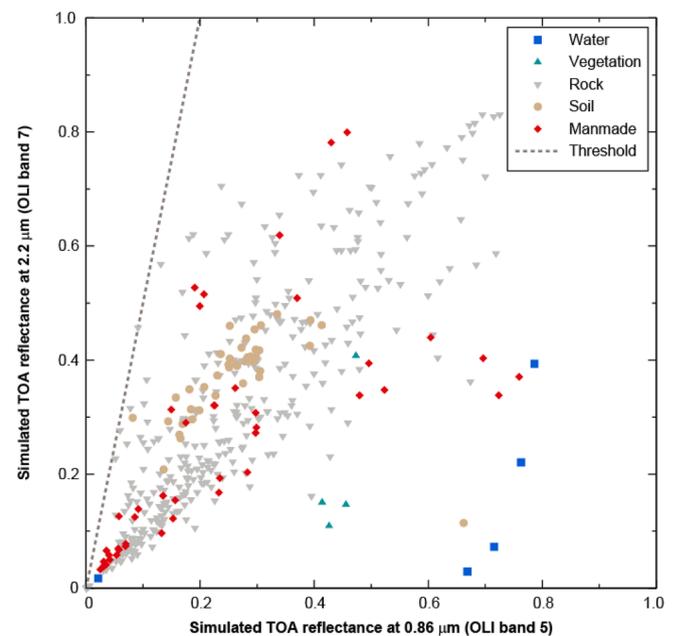

Fig. 2. Comparison between TOA reflectances of land surface materials at 0.86 μm and 2.2 μm simulated based on the samples from the ASTER spectral library (Baldridge et al., 2009) using the U.S. standard atmospheric model. The dotted line indicates the detection threshold of Eq. (1).

decrease the commission error rate, we attenuated the detection sensitivity by omitting contextual analysis to detect small fire, such as proposed by Schroeder et al. (2016), and by using a looser threshold for SWIR to NIR ratio relative to the methods proposed by Schroeder et al. (2016), Murphy et al. (2016), Kumar and Roy (2018), and Sofan et al. (2019).

The detection conditions are

$$R_{SWIR2}/R_{NIR} > 5.0, \tag{1}$$

$$R_{NIR} < 0.38 \tag{2}$$

and

$$L_{SWIR2} > 5.28 \tag{3}$$

where R_{NIR} and R_{SWIR2} are the Top of Atmosphere (TOA) reflectances at 0.86 μm and 2.2 μm wavelengths, respectively. L_{SWIR2} is TOA radiance at the 2.2 μm band in W/m^2 μm sr.

(a) Sentinel-2A MSI Band 12 on January 4, 2016   (b) Landsat 8 OLI band 7 on December 28, 2015

(c) Sentinel-2A MSI true color on January 4, 2016   (d) Landsat 8 OLI true color on December 28, 2015
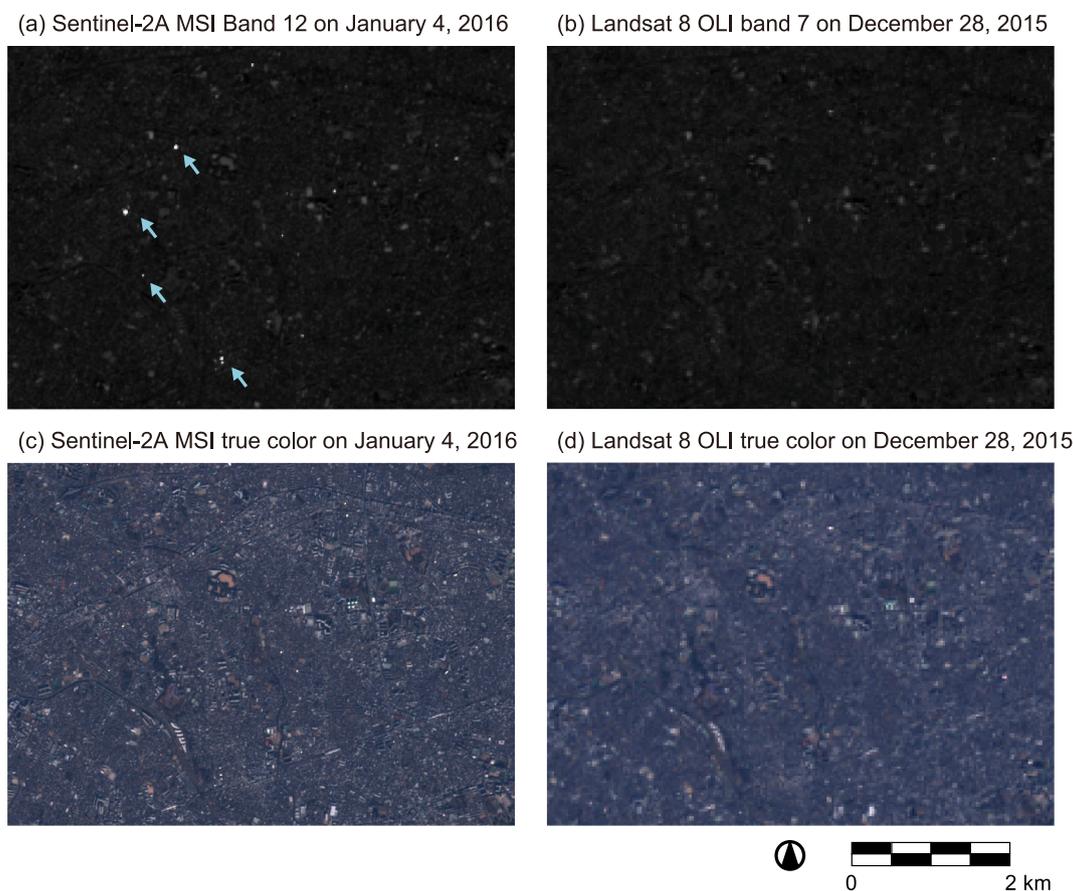

0   2 km

Fig. 3. Example of specular reflection on building roofs that is significant on MSI imagery. The images show TOA reflectance scaled from 0 to 1 in 2.2 μm band of (a) Sentinel-2A MSI and (b) Landsat 8 OLI and true color images taken by (c) Sentinel-2 MSI and (d) Landsat 8 OLI in a suburb of Tokyo, Japan (54SUE on the Sentinel-2 tiling system) on January 4, 2016 and December 28, 2015, respectively. The arrows in (a) indicate pixels corresponding to specular reflection that satisfy Eq. (1) but are excluded by Eq. (4).

Although these bands are reflective bands, a thermal anomaly, such as an active fire, increases the apparent SWIR reflectance whereas spectral radiance from very hot targets is insignificant in NIR region. A key idea of Eq. (1), originally proposed by Giglio et al. (2008), is to distinguish pixels with anomalously high apparent SWIR reflectance due to substantial emission. The empirical coefficient for Eq. (1) was determined from simulated TOA reflectances of several surface materials from the ASTER spectral library (Baldridge et al., 2009). Atmospheric effects were estimated by MODTRAN 5 using the U.S. standard atmosphere and then convolved to the spectral responses of OLI bands. As Fig. 2 shows, TOA reflectances at OLI band 7 are comparable to or up to 5 times of those at band 5 except for water and vegetation. Assuming the observed spectral radiance is composed of reflected solar radiance and radiance emitted from very hot heat source, we determined a threshold line shown in Fig. 2 to distinguish pixels receiving a significant amount of SWIR radiance from the pixels with only reflected radiance signal. As such our targets do not include lower temperature thermal anomalies such as sub-boiling hot springs and volcanic crater lakes.

Eq. (2) excludes pixels with high NIR reflectance to eliminate commission error associate with the contamination of cloud and occasional specular reflection from relatively flat slope surface, which is more significant in longer wavelength (Bennett and Porteus, 1961). In addition, Eq. (3) discards pixels which are corresponding to small spectral radiance often occurs on water bodies. The thresholds for these two equations were manually optimized by inspecting several OLI and MSI scenes.

Specular reflection from flat slopes, such as roofs and solar panels, is frequently observed in the MSI data due to finer spatial resolution. Fig. 3 shows a typical example of specular reflection from building roofs.

Although TOA reflectance in the visible region is similar between OLI and MSI, several bright spots are seen on MSI SWIR image in the same season. Therefore, we introduced an additional threshold test to distinguish thermal anomalies from specular reflection only for MSI data, assuming reflectance at 1.6 μm correlates with reflectances at 0.87 μm and 2.2 μm:

$$1.65 < \frac{R_{SWIR2} - R_{NIR}}{R_{SWIR1} - R_{NIR}} < 33 \tag{4}$$

where R_{SWIR1} is TOA reflectance in the 1.6 μm band. This threshold test evaluates whether the apparent NIR-SWIR spectrum falls within the temperature range of hot target. Assuming spectrally flat reflectance in the NIR to SWIR region, Eq. (4) indicates a ratio between spectral radiance from a heat source at 2.2 μm to 1.6 μm. The lower and upper thresholds are corresponding to blackbody radiance at temperatures of 2500 K and 600 K, which approximate a temperature range of thermal anomalies. Because a larger solar zenith angle increases the occurrence of specular reflection, for scenes observed in winter, the upper threshold is decreased to 3.0 (corresponding to 1500 K) for detected results composed of less than four adjacent pixels. Fig. 3(a) indicates pixels corresponding to specular reflection that satisfy Eq. (1) but are excluded by Eq. (4).

OLI occasionally conducts observation at nighttime to, for example, monitor volcanic activities. Lack of solar input allows to simplify the detection equations as
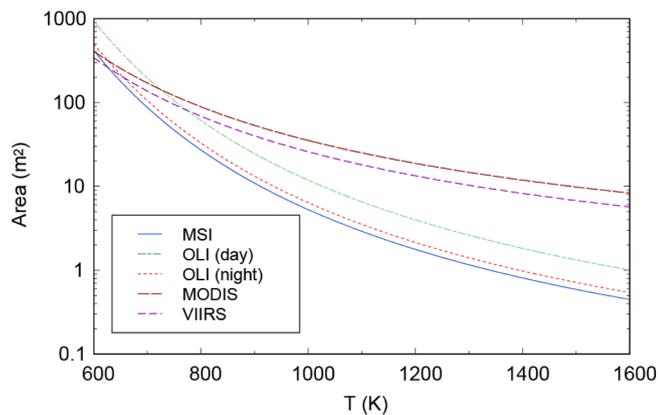
$$L_{SWIR2} > 2.64 \tag{5}$$

and

Fig. 4. The combination of brightness temperature and area equivalent to the detection threshold assuming a hotspot composed of one pixel with background radiance corresponding to 0.015 of apparent reflectance in the 2.2 μm band for daytime OLI and MSI and no background radiance for nighttime OLI simulations. Curves for the MODIS and VIIRS data are drawn based on the minimum allowable radiances for their fire detection algorithms, namely equivalent to the brightness temperature of 298 K (background temperature + 5 K) and 320 K in their nominal spatial resolutions, respectively, in the 4 μm band (Giglio et al., 2016; Schroeder et al., 2014; respectively) considering background surface temperature of 293 K.

$$L_{NIR}/L_{SWIR2} < 0.2 \qquad (6)$$

Both equations test whether the observed spectral radiances fall within the temperature range of hot target. The threshold in Eq. (5) roughly corresponds to a spectral blackbody radiance from a hotspot of 1 m^2 with a temperature of 950 K at 30-m resolution. To avoid false detection due to lights in urban areas, Eq. (6) selects only pixels corresponding to a blackbody temperature below 1600 K.

Adjacent hotspot pixels often correspond to the same heat source, e. g., a curvilinearly extended fire front of a wildfire, or a point heat source smeared by geometric correction. To treat such multi-pixel hotspots, we aggregate adjacent or neighboring hotspot pixels up to a 2.5 km distance.

Fig. 4 shows simulated detectable minimums of hotspot temperature and subpixel area under ideal conditions, in which a single heat source exists within one pixel under negligible atmospheric effect, for both daytime and nighttime. Note that this comparison only represents a particular scenario described below because the minimum limits of temperature and size of hotspot depend on regional factors including spectral reflectance and surface temperature of surroundings. The daytime simulation assumed a shaded surface—reflectance as low as 0.015 in the 2.2 μm band—because Eq. (3) cannot be satisfied together with Eq. (1) under sunlit conditions. The smearing effect due to orthorectification is considered to simulate a hotspot on a geometrically corrected product. For comparison purposes, Fig. 4 also indicates the detectable minimums of the MODIS and VIIRS active fire algorithms, in accordance with brightness temperatures of 298 K (background temperature + 5 K) and 320 K in the 4 μm band at the nominal spatial resolutions, 1 km and 375 m, respectively (Giglio et al., 2016; Schroeder et al., 2014) considering 293 K of background surface temperature.

Under this specific condition, OLI and MSI have the advantage of a higher spatial resolution to detect smaller hotspots at relatively high temperatures compared with MODIS and VIIRS. For example, in a daytime simulation, a hotspot of about 12 m^2 and 5 m^2 can be detected by OLI and MSI, respectively, when the hotspot temperature reaches 1000 K; in contrast MODIS and VIIRS can detect a hotspot of over 35 m^2 and 26 m^2, respectively. The finer spatial resolution of the MSI enables detection of hotspots half as large as those that OLI can detect. At nighttime, the lack of reflected solar radiance decreases the size of the detectable hotspot to about half of that under daytime conditions. As

such, the thresholds for OLI and MSI data are sufficient to detect very hot but small size targets, such as a few m^2 of fire.

2.2. Heat source classification

The hotspot detection descried in Section 2.1 relies on the observed spectral radiance attributed to the high-temperature heat sources which include, for instance, biomass burning, volcanic activity, and industrial activity. Detected hotspots from the high-temperature heat sources investigated here also include some false detections. Contemporary image recognition techniques based on CNN, as a widely used deep learning algorithm to classify images exploring spatially discriminative shape/texture features, are especially efficient at automatically classifying heat sources semantically on a global scale (Ma et al., 2019). The CNN-based classification could potentially be an alternative to visual inspection by human experts. We assumed that heat sources have strong correlation with surrounding background, e.g., wildfires with vegetated areas and industrial activities with urban areas. Although the most heat sources are subpixel-sized in 20 to 30-m resolution, CNN would associate typical features in surrounding background with the heat source category. Even if CNN ideally learned the spatial features of the ground surface, mislabeling would often occur for images affected by clouds, plumes, or shadows. Existing land use/land cover layers are applicable as secondary references, although they are temporally inconsistent with the detected hotspots. Moreover, spatial coincidence in multi-temporal hotspot detection provides insight to distinguish among heat sources as Schroeder et al. (2016) and Kumar and Roy (2018) applied multitemporal commission error reduction tests using co-located data in past 176 days. A traditional decision tree approach is suitable for implementing the temporal context and GIS-based classification. This study applied the CNN-based and the decision tree-based classifications independently, and then combined their results to increase classification reliability.

Both classification methods need training samples. We selected a variety of different hotspots from global regions from April 2013 to October 2016, as shown in Table 2 and Fig. 5. They were classified into eight categories—volcano, factory, oil platform, fire (forest), fire (grass), fire (urban), false detection by specular reflection, and non-typable—by visually inspecting satellite images from before and after the detection of the hotspot and maps and high-resolution aerial photos on Google Maps. Despite geographically diverse samples, specular reflection was mostly located in China, due to concentration of large factories with perhaps locally dominant roof materials, which Schroeder et al. (2016) pointed out. Such geographical bias in training data could cause overfitting in the CNN-based method which reduces the classification accuracy.

2.2.1. CNN-based classification

Training a CNN network needs labeled patch images. Although the hotspot detection uses only two or three bands of multispectral data, patch images were created from seven bands including the visible region—namely bands 1 to 7 for OLI and bands 1 to 4, 8A, 11, and 12 for MSI—to utilize spatial context on the background land surface as much as possible. To make the CNN focus on the features corresponding to
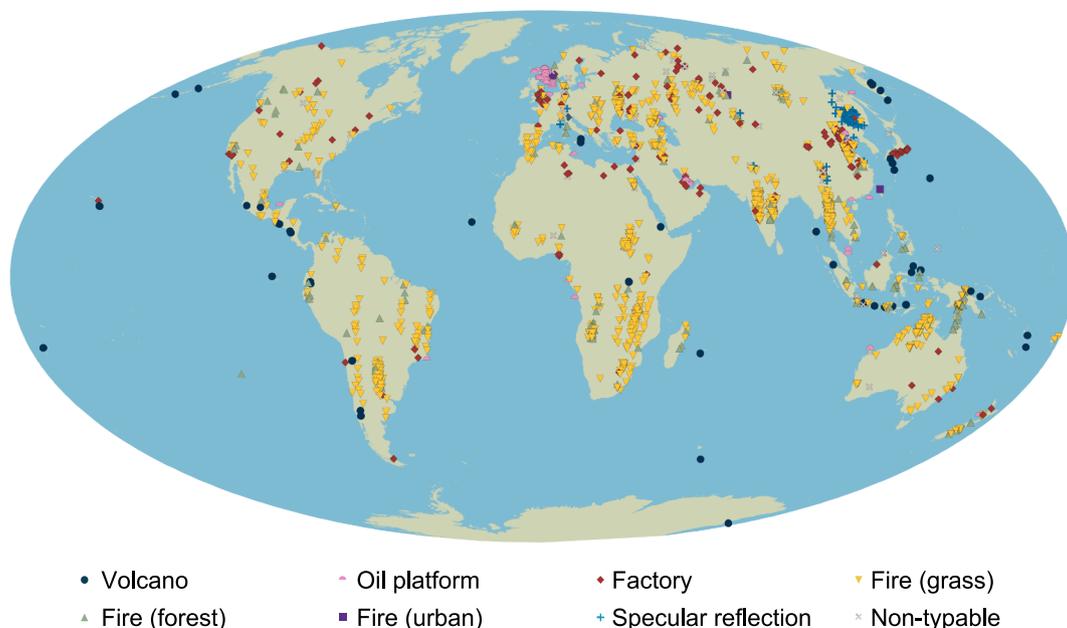
Table 2
Summary of the training samples for classifying hotspots.

Reference category	Number of training data
Volcano	225
Factory	246
Oil platform	198
Fire (grass)	1340
Fire (forest)	336
Fire (urban)	3
Specular reflection	106
Non-typable	62
Total	2516

- • Volcano
- ⌒ Oil platform
- ◆ Factory
- ▽ Fire (grass)
- △ Fire (forest)
- ■ Fire (urban)
- + Specular reflection
- × Non-typable

Fig. 5. Location of the training samples selected from April 2013 to October 2016.
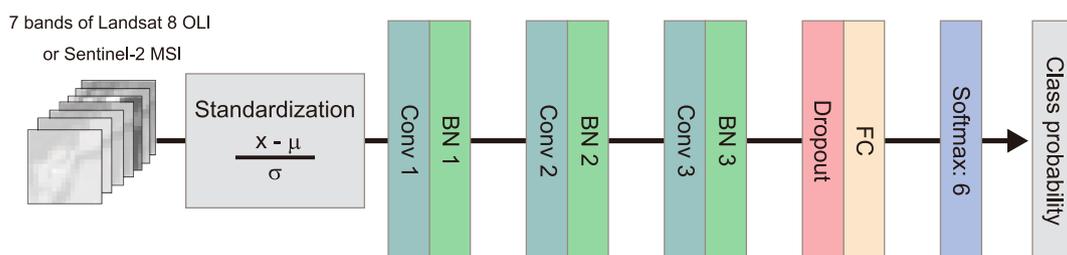

Fig. 6. Architecture of the CNN model. Input data are composed of bands 1–7 for OLI and bands 1–4, 8A, 11, and 12 for MSI. Conv, convolution layer; BN, batch normalization layer; FC, fully connected layer; x, digital number; μ, mean digital number within training data; σ, standard deviation of digital number within training data.

heat sources, satellite images were clipped into 16×16 pixels at 30 m spatial resolution, which is smaller than generally used for image recognition (e.g., Xu et al., 2018). MSI data at 60 m spatial resolution for band 1, 10 m spatial resolution for bands 2 to 4, and 20 m spatial resolution for bands 8A, 11, and 12 were resampled into 30 m spatial resolution using bilinear interpolation so as to share the CNN model with OLI. The CNN-based method is applied only for daytime data. The categories fire (forest) and fire (grass) were merged into one category, fire, because of the ambiguity in spectral patterns. Fire (urban) was omitted owing to the limited number of training data.

To classify the patch images into the six categories mentioned above, we used a simple CNN model composed of three convolution layers with a fully connected (FC) layer, modifying a CNN model constructed to detect photovoltaic power plants from satellite imagery (Ishii et al., 2016). Each convolutional layer uses 3×3 kernels with stride 1 without padding and is followed by a Rectified Linear Unit (ReLU) activation layer. No pooling layer was used because the size of the input patch image was small. For training, batch normalization was used between each convolution layer and ReLU activation layer. Before the fully connected layer, a dropout layer sets the output pixels to 0 with 50% possibility to reduce model overfitting to the training data. The category with the largest probability is finally selected as the classification result (Fig. 6).

2.2.2. Decision tree-based classification

We propose an additional classification method based on thematic datasets—namely global land cover and volcanic database—and our own archival hotspot records to overcome classification errors by the CNN-based method. As a global land cover map, we used the European Space Agency Climate Change Initiative Land Cover (ESACCILC) dataset with 300 m spatial resolution (ESA, 2017). Although ESA provides annual representative land cover maps from 1992 to 2018, we only used the land cover map for 2015 as a representative for our study period. In addition, we used geographic coordinates for volcanoes from the Image Database for Volcanoes (Urai, 2011).

Our decision tree also utilized the detection history for the location of hotspots. Because data acquisition opportunities are limited by cloud coverage in addition to the revisit cycle of the satellites, we focused on the seasonality of the repeatedly detected hotspots instead of the frequency of their detection. As a seasonality index, a monthly histogram was calculated for the detected hotspots regardless of year within a 1 km square area around a hotspot to be classified.

Our classification is based on the following assumptions: (1) hotspots located within 5 km of a volcanic vent correspond to lava flow, (2) industrial activities have no seasonality, (3) agricultural open burnings are conducted every 6 months with a 3-month active period, (4) specular reflection occurs up to twice a year over the same place during the solar zenith angle of 45° to 55°, (5) oil platforms are lost in water bodies on coarse ESACCILC, (6) wildfires occur randomly in terms of location, (7) man-made objects witch cause specular reflection are smaller than 4500 m^2, and (8) impervious surfaces can be confused with bare soil on ESACCILC due to ambiguous surface spectra.
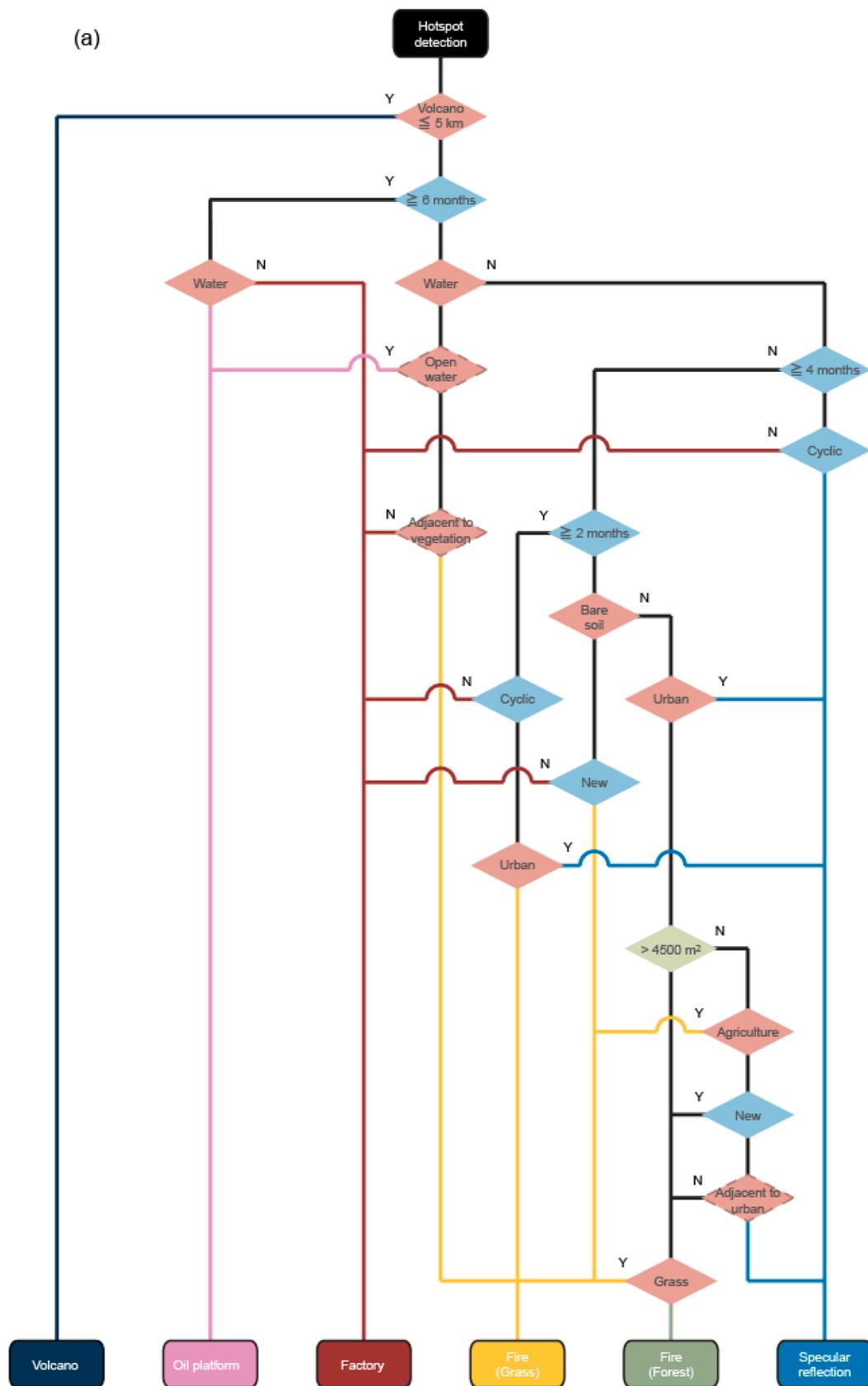
Fig. 7. Decision tree-based classification of the detected hotspots for (a) daytime and (b) nighttime data. Red, blue, and green diamonds indicate decisions based on land cover, seasonality or frequency, and size, respectively.
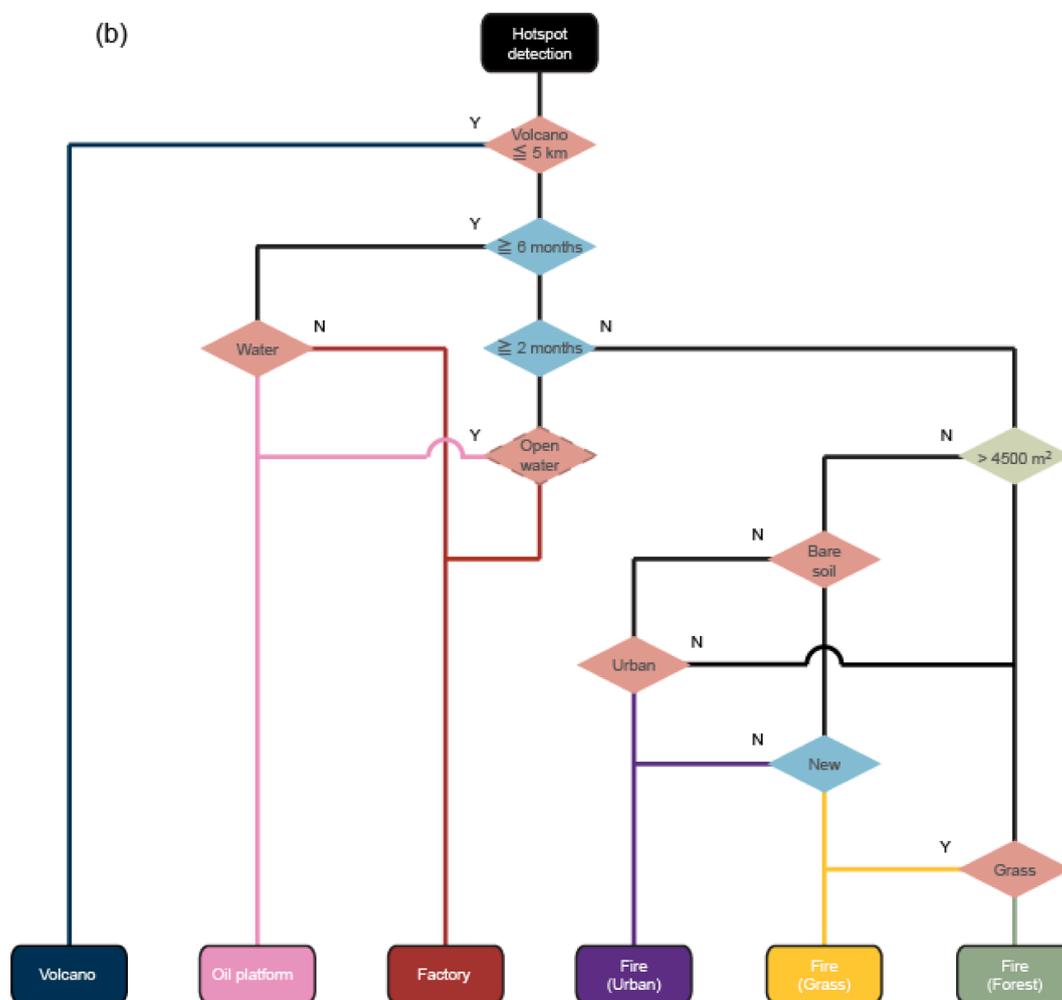
Fig. 7. (*continued*).

Table 3
Summary of the validation samples for classifying hotspots. The numbers of samples were based on the decision tree-based classification.

Category (classified by the decision tree-based method)	Number of validation data		
	The two classification methods concurred	The two classification methods conflicted	Total
Volcano	517	148	665
Factory	1087	435	1522
Oil platform	1036	182	1218
Fire (grass)	1001	446	1447
Fire (forest)	1000	336	1336
Specular reflection	4553	218	4771
Total	9194	1765	10,959

Using the training dataset, we decided the decision rules to classify daytime hotspot data into volcano, oil platform, factory, fire (grass), fire (forest), and specular reflection (Fig. 7a). For nighttime data, hotspots detected in urban areas are classified to fire (urban), which can occur even during daytime but are unrecognizable based only on the data we used (Fig. 7b).

Despite each decision rule having individual constraints—for example, assumption (1) causes misclassification of wildfire within 5 km of a volcanic vent as volcano—the thresholds for the decision rules were determined to minimize classification error.

3. Results and discussion

3.1. Validation and enhancement of daytime classification results

This section evaluated classification accuracies of the two classification methods. The outcome of the statistical validation revealed which method was more appropriate for each classified category or tendencies of misclassification corresponding to specific combinations of the two classification results. We subsequently discussed how to improve classification accuracy when one or both of classification methods tended to fail.

The classification results from both methods were validated using 10,959 samples selected from 1,044,680 hotspots detected using daytime OLI data from May 2017 to July 2019 (Table 3). We selected samples for which the two classification results agreed and disagreed separately because the two classification results agreed well (79.7% in total; Fig. 8), except for specular refection. Note that we assumed that fire by the CNN-based classification was comparable with both fire (grass) and fire (forest) by the decision tree-based method. Selected samples were validated by the visual inspection as with the training samples.

To validate agreed results, we selected about 1000 samples for each category excluding volcanoes and specular reflection for which we validated all the classification results during the studied period (Table 3). This analysis omitted the category "non-typable" which represented ambiguous images only for the CNN-based method. Hotspots where the two different classification results agreed were accurately
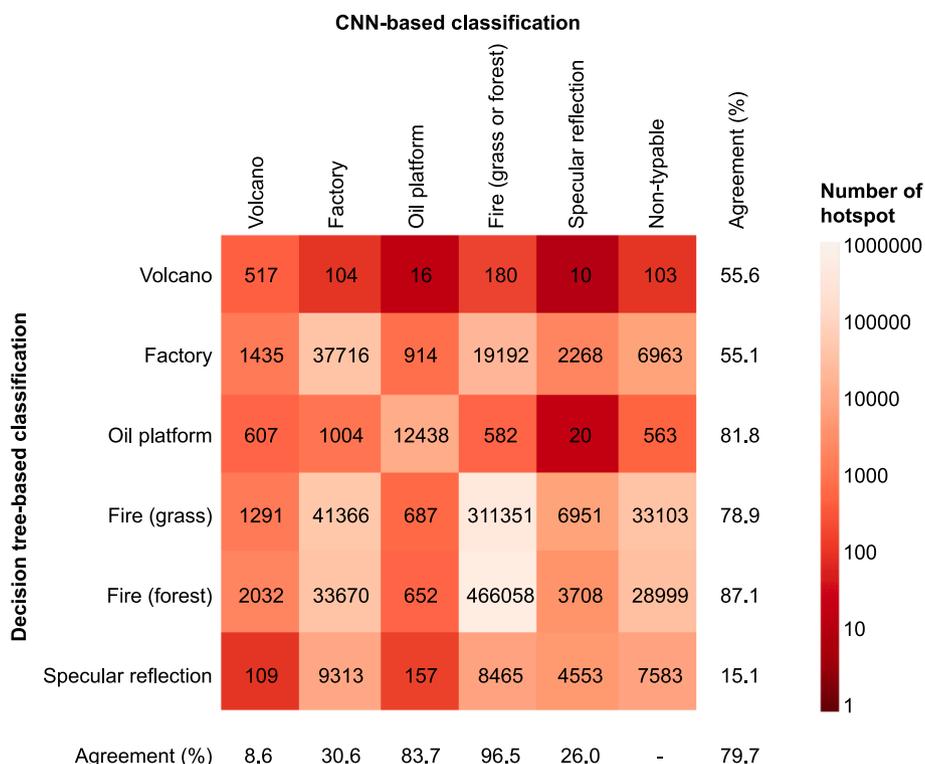
CNN-based classification

	Volcano	Factory	Oil platform	Fire (grass or forest)	Specular reflection	Non-typable	Agreement (%)
Volcano	517	104	16	180	10	103	55.6
Factory	1435	37716	914	19192	2268	6963	55.1
Oil platform	607	1004	12438	582	20	563	81.8
Fire (grass)	1291	41366	687	311351	6951	33103	78.9
Fire (forest)	2032	33670	652	466058	3708	28999	87.1
Specular reflection	109	9313	157	8465	4553	7583	15.1
Agreement (%)	8.6	30.6	83.7	96.5	26.0	-	79.7

(Decision tree-based classification — row axis label)

Number of hotspot: 1000000, 100000, 10000, 1000, 100, 10, 1

Fig. 8. Agreement matrix between the classification results from the CNN-based and the decision tree-based methods for hotspots detected from May 2017 to July 2019.
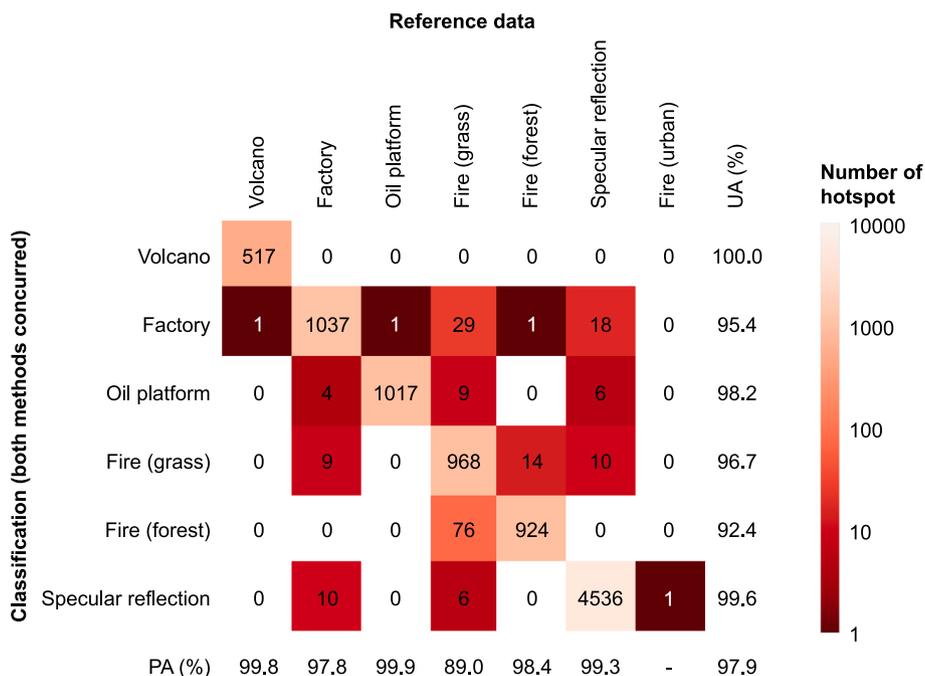
Reference data

	Volcano	Factory	Oil platform	Fire (grass)	Fire (forest)	Specular reflection	Fire (urban)	UA (%)
Volcano	517	0	0	0	0	0	0	100.0
Factory	1	1037	1	29	1	18	0	95.4
Oil platform	0	4	1017	9	0	6	0	98.2
Fire (grass)	0	9	0	968	14	10	0	96.7
Fire (forest)	0	0	0	76	924	0	0	92.4
Specular reflection	0	10	0	6	0	4536	1	99.6
PA (%)	99.8	97.8	99.9	89.0	98.4	99.3	-	97.9

(Classification (both methods concurred) — row axis label)

Number of hotspot: 10000, 1000, 100, 10, 1

Fig. 9. Validation of the classified hotspots where the CNN-based and the decision tree-based methods concurred, from May 2017 to July 2019. UA, user's accuracy; PA, producer's accuracy.

classified in 97.9% of cases (Fig. 9). The lowest user's and producer's accuracies were corresponding respectively to fire (forest) and fire (grass). These two categories were often mutually confused by the decision tree-based method because boundaries between forest and grass were lost in the relatively coarse ESACCILC. Taking vegetation fire as a single category, the user's and producer's accuracies would increase to

99.1% and 97.8%, respectively.

Fig. 10 shows typical positive and negative examples where both methods concurred. As seen from these examples, relatively large hotspots are apparent as their labeled categories. Small hotspots were often mislabeled because the background surface relatively represents the chip image for the CNN-based classification while small areas are often
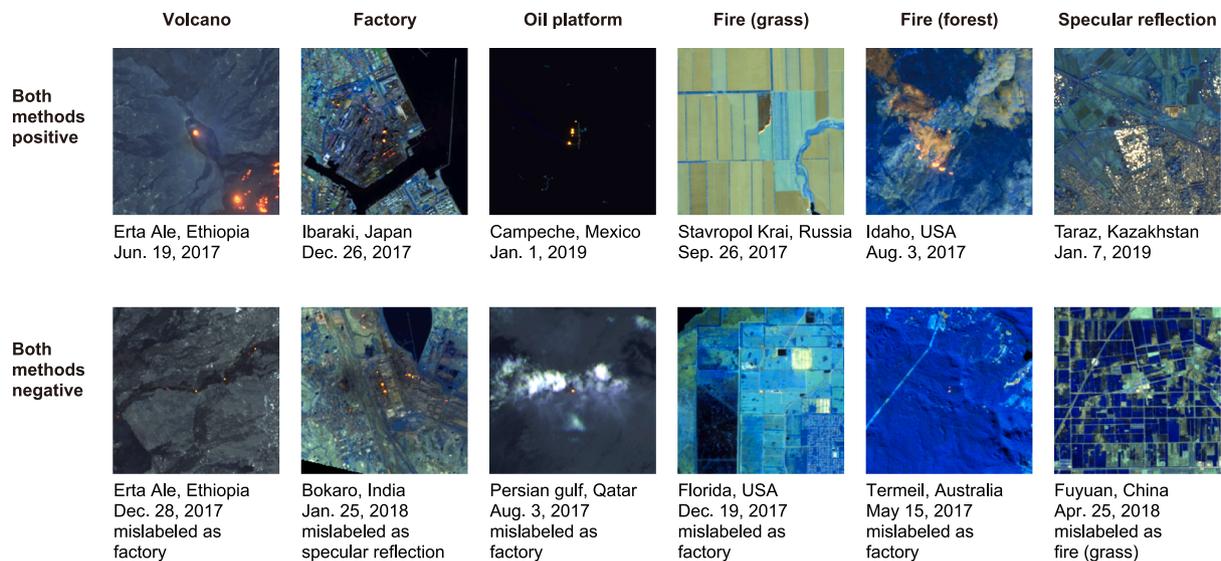
Fig. 10. Examples of typical hotspots where the CNN-based and the decision tree-based methods concurred. Each image is composed of RGB: 765 covering a 6 km × 6 km area around the most significant hotspot pixel within the adjacent detected pixels on OLI images.
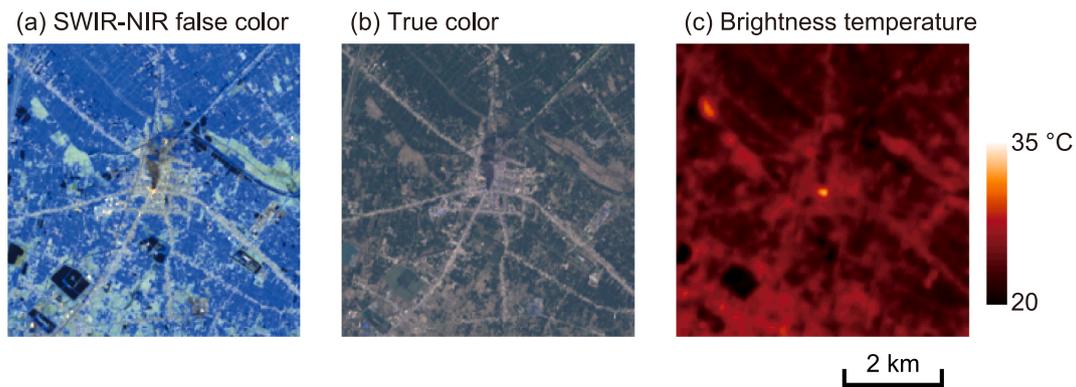

Fig. 11. (a) False color image composed of RGB: 765, (b) true color image composed of RGB: 432, and (c) pseudo color image for TOA brightness temperature based on band 10 for an urban fire that occurred in Anhui, China (path/row = 122/037) captured by Landsat 8 on April 17, 2018 and classified as specular reflection by both the CNN-based and decision tre-based methods.

unrecognizable in ESACCILC. Repeatedly occurred hotspots are often confused with factory by the decision tree-based method. In contrast, genuine factories can be misclassified into specular reflection when detected only in limited seasons.

In samples classified as specular reflection, we found an urban fire, where dark smoke from the hotspot was obvious on both the visible and infrared images and the thermal infrared image (band 10) also implied a thermal anomaly (Fig. 11). Even if urban fires as visually evident as in this example are detected accidentally, the current classification procedure inevitably labels them as specular reflection owing to the statistically insufficient amount of training data.

We also evaluated the classification results where the two classification methods conflicted, examples of which are shown in Fig. 12. The fact that the decision tree-based method resulted in relatively accurate classification implied that the detection frequency or pixel-based land use type relatively represented the characteristic of the heat source. In the validated samples, 27% were corresponding to hotspots where both methods failed, mostly due to irregular locations such as coastal areas. Fig. 13 shows a confusion matrix between reference data and a combination of the two classification results prioritizing the decision tree-based method over the CNN-based method. Fig. 13 also shows the most probable categories and their probabilities corresponding to the combination of the two classification methods. When the two

classification results conflicted, replacing the category with the most probable category improves the classification accuracy, or correct for biases in the classification results to some extent. This correction scheme increases the overall accuracy from 54.8% and 18.1% for the individual classification methods based on the decision tree and the CNN, respectively, to 66.2% in total (Fig. 14). However, decrease in F score shows that the combined classification resulted in poorer accuracy in classifying fire (forest) than the decision tree-based method, which compensated by increased accuracy in classifying fire (grass). As shown in Fig. 13, fire (grass) reclassed from fire (forest) were mostly corresponding to grass or forest in comparable contribution. Because the samples are not statistically sufficient for some combinations of classification category, we intend to increase the number of cases in a future study. Combining the CNN-based and decision tree-based results achieved an overall accuracy of 92.8% for daytime data.

3.2. Validation of nighttime classification results

Classification results for nighttime OLI data were validated using 2,386 samples obtained during May 2017 through January 2019. The validated samples include all the results classified as oil platform and volcano because there were only 42 and 214 cases, respectively. As summarized in Fig. 15, the overall accuracy reached 79.3%.
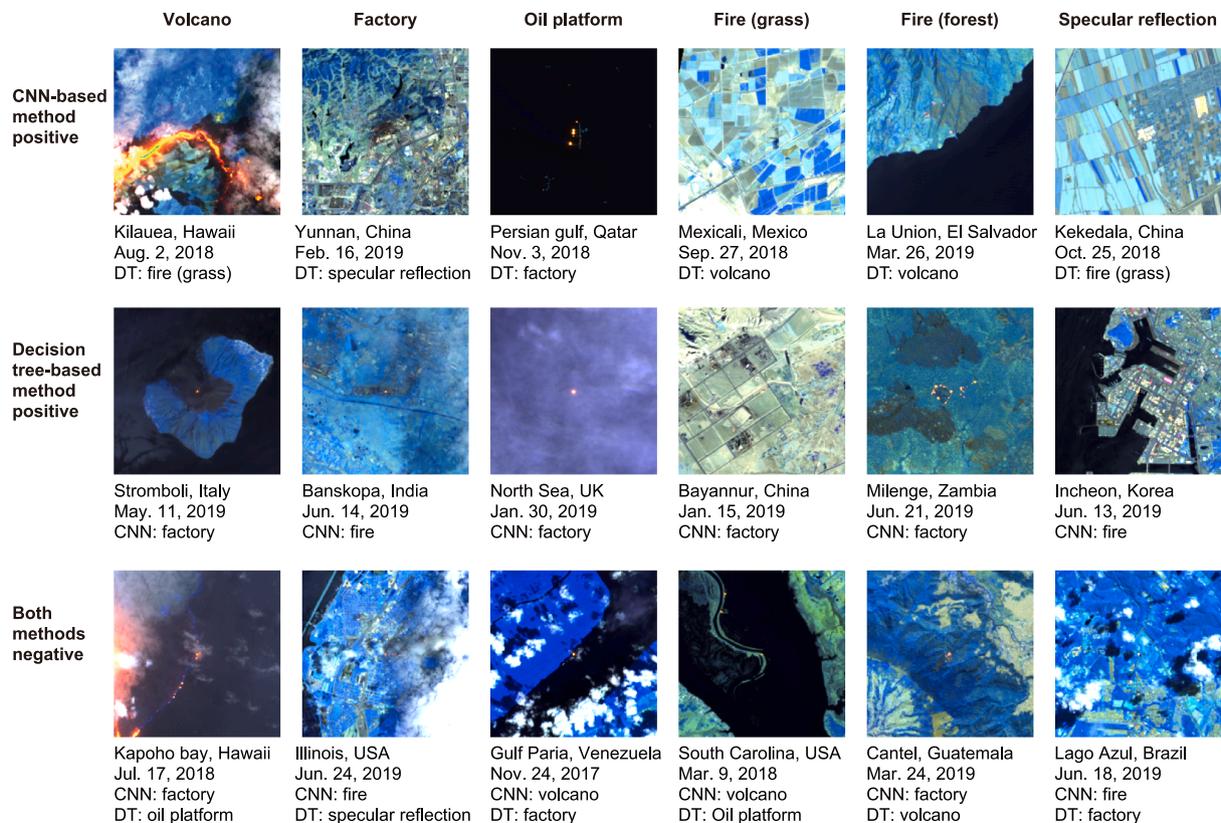
Fig. 12. Examples of typical hotspots where the CNN-based and the decision tree-based methods conflicted. Each image is composed of RGB: 765 covering a 6 km × 6 km area around the most significant hotspot pixel within the adjacent detected pixels on OLI images. CNN, CNN-based method; DT, decision tree-based method.

Classifications of volcano, factory, fire (grass), and fire (urban) were relatively accurate as both user's and producer's accuracy exceeded 70%. Whereas oil platforms were accurately classified from daytime data, coastal industrial facilities were often mislabeled as oil platforms with nighttime data. Only eight genuine oil platforms were found because offshore areas are usually not scheduled to be observed at nighttime. More than 20% of the factories, mostly inland oil and gas plants in North America, were classified as fire (forest), fire (urban), or fire (grass). Because these industrial facilities were detected only once or twice with nighttime data, they were classified based only on coarse land cover information. More data are necessary to enhance the classification accuracy for nighttime hotspots.

3.3. Validation with the VIIRS fire products

We have been applying our hotspot detection to all Landsat 8 OLI scenes from the beginning of the operation that have been released through Amazon Web Services (AWS). Our WebGIS site (https://gsrt.airc.aist.go.jp/hotarea/) visualizes automatically detected and classified results. Although our hotspot detection is applied on a global scale using OLI data, the 16-day revisit interval limits the opportunity to comprehensively acquire fire events. We evaluated detection effectiveness according to daytime acquisition of OLI by comparing the detection frequency with the VIIRS fire product, which has the highest ability with respect to hotspot detection. This section discusses only the results obtained by daytime OLI data because nighttime OLI acquisition is limited and we have demonstrated MSI data for selected regions since January 2018. We compared annual spatial distributions of hotspots qualitatively because the sensitivity to thermal anomalies, the spatial resolution, revisit interval, and acquisition time are different between the sensors. The annual frequencies of thermal anomalies during 2018, approximated by the number of detected pixels per 100-km radius area, were mapped according to daytime OLI data (Fig. 16) and VIIRS active

fire product (Fig. 17). For this comparison, we excluded hotspots classified as specular reflection based on the procedure outlined in Section 3.1.

Despite the limited observation opportunities, the thermal anomalies derived by OLI indicated similar regional tendencies when compared with VIIRS. Most noticeably, frequent and broad thermal anomalies occurred in Africa, north-western Australia, northern China, and South America. Both maps showed the same peak locations in North America, the Middle East, the Russian Far East, and the Indochina peninsula.

Cloud coverage would have decreased the chance of detection over the middle of tropical rain forests in Africa, South America, and Kalimantan island. Except for areas affected by cloud coverage, deserts, and permanently frozen areas, hotspots were detected in most land surfaces at least once annually.

Additionally, we investigated small-scale hotspots undetectable by VIIRS, implied in Section 2.1. Due to the differences in acquisition time between OLI and VIIRS, it is difficult to simultaneously observe the same hotspot by both sensors from a nadir view. As stable small heat sources, we searched for hotspots corresponding to 1 pixel classified as factory which had never been detected by VIIRS during 2014 to 2018. Visual inspection identified 149 hotspots as genuine industrial facilities including flare stacks, mines, incineration plants, landfill gas power plants, metal processing factories, liquefied natural gas terminals, chemical factories, wood production factories, wastewater treatment plants, cement factories, ironworks, and petroleum facilities. Detection of these small hotspots implies that OLI has sensitivity for small and hot heat sources as expected. Small-scale active fire and volcanic activity would have been detected by our system as well.

4. Conclusions

We developed a hotspot classification system combining the CNN-based and the decision tree-based classifiers for Landsat 8 OLI and
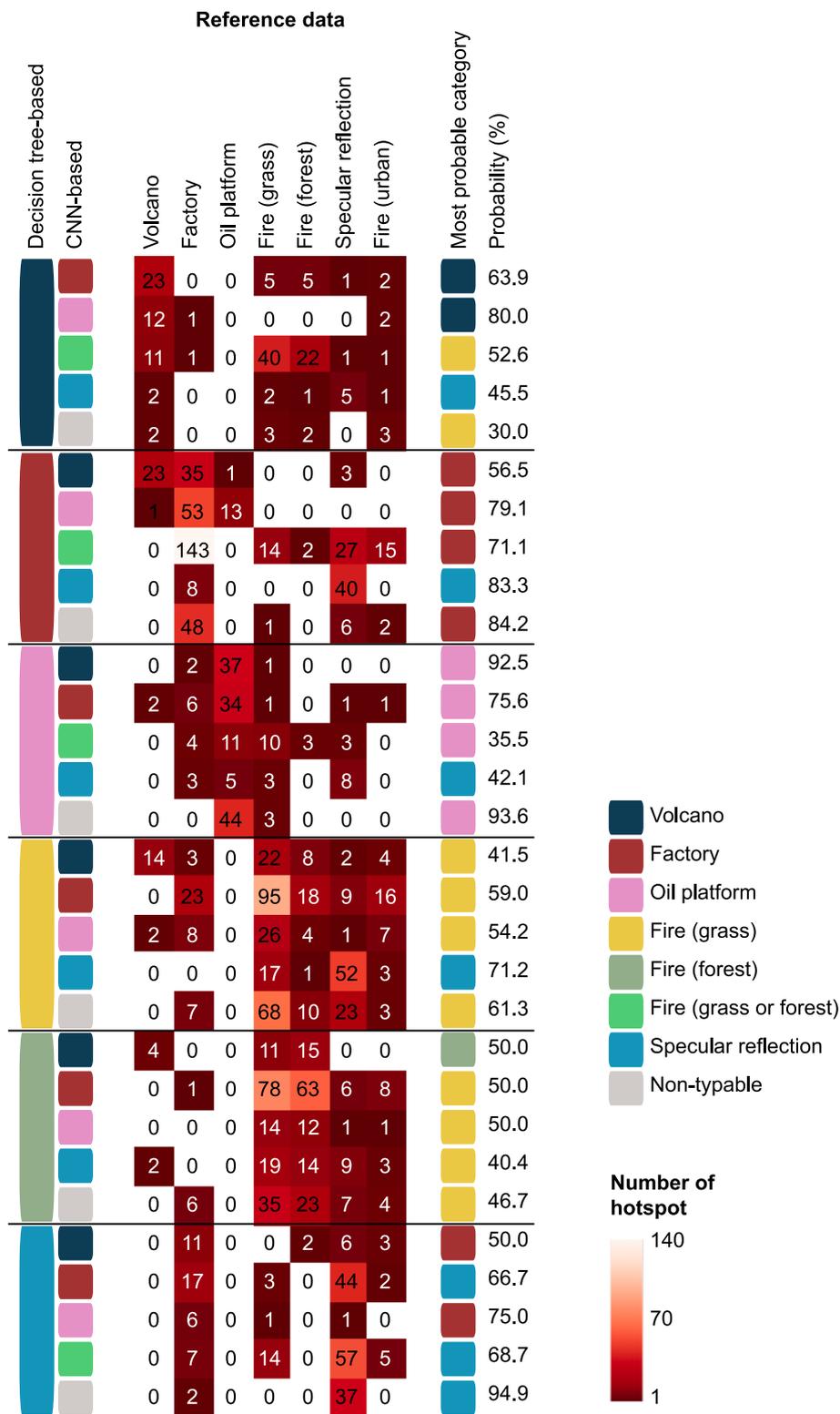
Fig. 13. Validation summary of classification results where the CNN-based and the decision tree-based methods conflicted, and the most probable category corresponding to the combination of the two classification results, from May 2017 to July 2019.

Sentinel-2 MSI data on a global scale. To develop and validate the classification method, geographically diverse training data were generated from Landsat 8 OLI data by a hotspot detection scheme which exploits anomalously high apparent SWIR reflectance corresponding to very hot targets. The daytime classification results between the CNN-based and the decision tree-based methods generally agreed well despite exploiting different information, namely shape/texture features and temporal pattern along with thematic land cover information, respectively. When both classification results agreed, overall accuracy of 97.9% was achieved. The agreement between the results from the two independent methods assured reliability of the classified results. Meanwhile, the decision tree-based method was relatively accurate
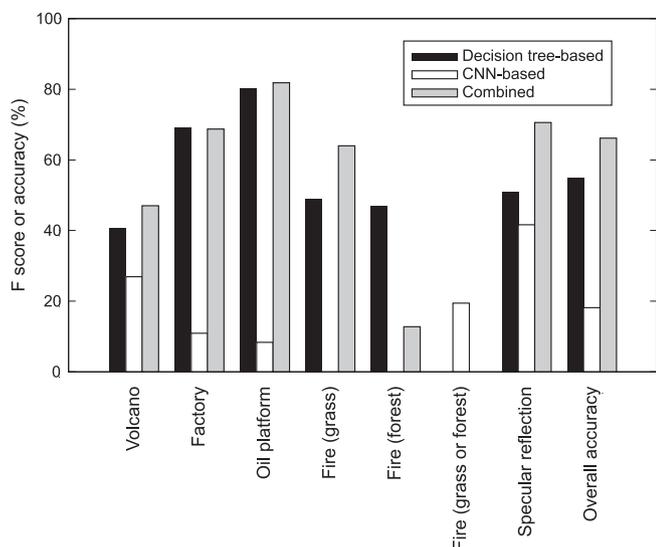
Fig. 14. F score for each classification category where the CNN-based and the decision tree-based methods conflicted and overall accuracy for decision-tree based, CNN-based and combined methods.

when the two classification methods conflicted. Such hotspots were re-classified into the most probable category according to the combination of the two classification results based on our validation study.

For nighttime scenes, only the decision tree-based method was used for the hotspot classification. In addition, the only a limited amount of nighttime OLI data were available to construct decision rules due to fewer observation opportunities. As a result, classification accuracy for nighttime data was only 79.3% whereas 92.8% of accuracy was achieved for daytime data.

The sensitivity to detect small and hot targets was confirmed by the fact that some OLI-derived small factories had not been detected by VIIRS. Although the MIR region, which VIIRS and MODIS fire algorithms

employ, is radiometrically most sensitive to thermal anomalies, higher spatial resolution is advantageous to detect small-sized hotspots.

One of the aims to classify heat source was to identify false detections due to specular reflection. Although such false detections were generally classified well, genuine fire events can be mislabeled as specular reflection by both classification methods depending on the sites of occurrence. Further investigation to enhance training data and classification schemes would be necessary to mitigate such deficit.

The revisit frequencies of OLI and MSI are too long to effectively monitor short-lived wildfires and volcanic events. In the near future, Landsat 9, Sentinel-2C and -2D are planned to be launched and will possibly increase observations suitable to detect hotspots. In addition, our scheme would be applicable to hyperspectral sensors, such as PRecursore IperSpettrale della Missione Applicativa (PRISMA) and Hyperspectral Imager SUIte (HISUI), both of which were launched in 2019, and the upcoming Hyperspectral Infrared Imager (HyspIRI), Environmental Mapping and Analysis Program (EnMAP) and Copernicus Hyperspectral Imaging Mission For The Environment (CHIME), which observe VNIR to SWIR spectra at a spatial resolution of 20 to 30 m on a global scale (Candela et al., 2016; Guanter et al., 2015; Lee et al., 2015; Matsunaga et al., 2019; Nieke and Rast, 2019). A data processing system capable of efficiently managing the huge amount of satellite data and detected/classified hotspots, based on e.g., cloud environment, is an additional challenge for further study.
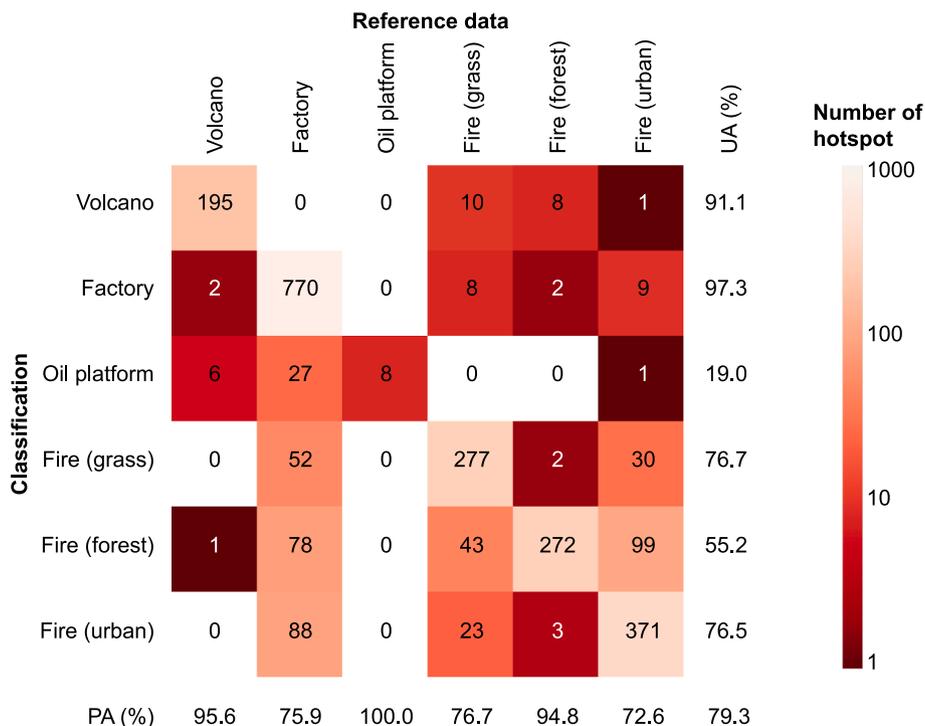
CRediT authorship contribution statement

Fig. 15. Validation summary of the decision tree-based classification of nighttime hotspots detected from May 2017 to January 2019. UA, user's accuracy; PA, producer's accuracy.
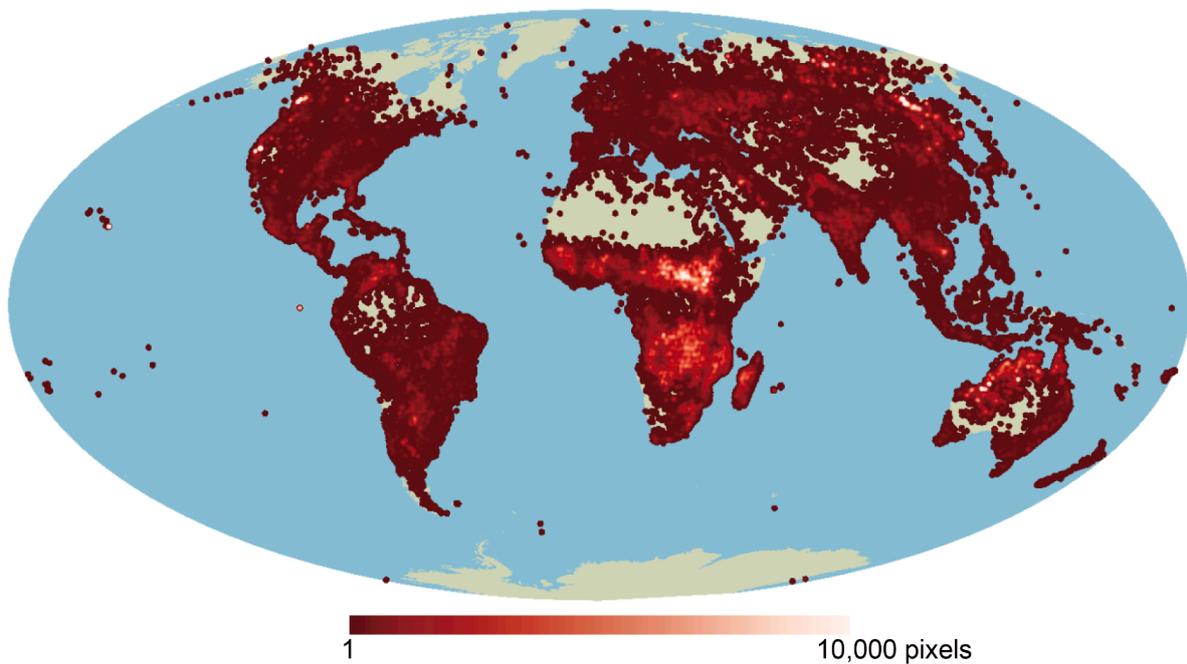
Fig. 16. Number of detected hotspot pixels (excluding specular reflection inferred from our classification procedure) from daytime OLI scenes during 2018. Heat maps were created corresponding to the number of detected pixels per 100-km radius area.
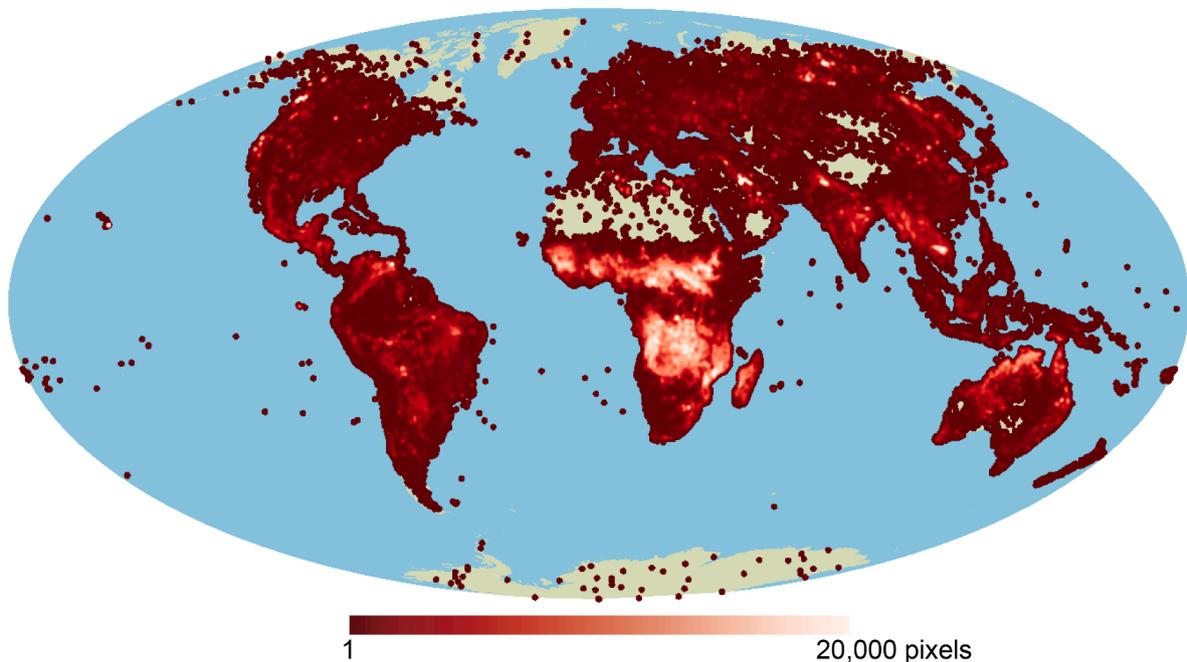

Fig. 17. Number of detected hotspot pixels from VIIRS data during 2018. Heat maps were created corresponding to the number of detected pixels per 100-km radius area.

Declaration of Competing Interest

The authors declare that they have no known competing financial interests or personal relationships that could have appeared to influence the work reported in this paper.

Acknowledgments

References

Baldridge, A.M., Hook, S.J., Grove, C.I., Rivera, G., 2009. The ASTER Spectral Library Version 2.0. Remote Sens. Environ. 113, 711–715.

Bennett, H.E., Porteus, J.O., 1961. Relation between surface roughness and specular reflectance at normal incidence. J. Opt. Soc. Am. 51, 123–129.

Boles, S.H., Verbyla, D.L., 2000. Comparison of Three AVHRR-Based Fire Detection Algorithms for Interior Alaska. Remote Sens. Environ. 72, 1–16.

Candela, L., Formaro, R., Guarini, R., Loizzo, R., Longo, F., Varacalli, G., 2016. The PRISMA mission. In: IEEE IGARSS 2016, Beijing, China, doi: 10.1109/ IGARSS.2016.7729057.

Davies, D.K., Ilavajhala, S., Wong, M.M., Justice, C.O., 2009. Fire Information for Resource Management System: Archiving and Distributing MODIS Active Fire Data. IEEE Trans. Geosci. Remote Sens. 47, 72–79.

ESA, 2017. Land Cover CCI Product User Guide Version 2.0, available at: http://maps.eli e.ucl.ac.be/CCI/viewer/download/ESACCI-LC-Ph2-PUGv2_2.0.pdf.

Flasse, S.P., Ceccato, P., 1996. A contextual algorithm for AVHRR fire detection. Int. J. Remote Sens. 17, 419–424.

Fukuhara, T., Kouyama, T., Kato, S., Nakamura, R., Takahashi, Y., Akiyama, H., 2017. Detection of small wildfire by thermal infrared camera with the uncooled microbolometer array for 50-kg class satellite. IEEE Trans. Geosci. Remote Sens. 55, 4314–4324.

Giglio, L., Descloitres, J., Justice, C.O., Kaufman, Y.J., 2003. An enhanced contextual fire detection algorithm for MODIS. Remote Sens. Environ. 87, 273–282.

Giglio, L., van der Werf, G.R., Randerson, J.T., Collatz, G.J., Kasibhatla, P., 2006. Global estimation of burned area using MODIS active fire observations. Atmos. Chem. Phys. 6, 957–974.

Giglio, L., Csiszar, I., Restás, Á., Morisette, J.T., Schroeder, W., Morton, D., Justice, C.O., 2008. Active fire detection and characterization with the Advanced Spaceborne Thermal Emission and Reflection Radiometer (ASTER). Remote Sens. Environ. 112, 3055–3063.

Giglio, L., Schroeder, W., Justice, C.O., 2016. The collection 6 MODIS active fire detection algorithm and fire products. Remote Sens. Environ. 178, 31–41.

Global Volcanism Program, 2013. Volcanoes of the World, v. 4.10.0 (14 May 2021). Venzke, E (Ed.), Smithsonian Institution. Downloaded 07 Jun 2021. https://doi.org/ 10.5479/si.GVP.VOTW4-2013.

Goss, M., Swain, D.L., Abatzoglou, J.T., Sarhadi, A., Kolden, C., Williams, A.P., Diffenbaugh, N.S., 2020. Climate change is increasing the risk of extreme autumn wildfire conditions across California. Environ. Res. Lett. 15 https://doi.org/ 10.1088/1748-9326/ab83a7.

Guanter, L., Kaufmann, H., Segl, K., Foerster, S., Rogass, C., Chabrillat, S., Kuester, T., Hollstein, A., Rossner, G., Chlebek, C., Straif, C., Fischer, S., Schrader, S., Storch, T., Heiden, U., Mueller, A., Bachmann, M., Mühle, H., Müller, R., Habermeyer, M., Ohndorf, A., Hill, J., Buddenbaum, H., Hostert, P., van der Linden, S., Leitão, P., Rabe, A., Doerffer, R., Krasemann, H., Xi, H., Mauser, W., Hank, T., Locherer, M., Rast, M., Staenz, K., Sang, B., 2015. The EnMAP spaceborne imaging spectroscopy mission for Earth observation. Remote Sens. 7, 8830–8857.

Halofsky, J.E., Peterson, D.L., Harvey, B.J., 2020. Changing wildfire, changing forests: the effects of climate change on fire regimes and vegetation in the Pacific Northwest, USA. Fire Ecol. 16 https://doi.org/10.1186/s42408-019-0062-8.

Hu, X., Ban, Y., Nascetti, A., 2021. Sentinel-2 MSI data for active fire detection in major fire-prone biomes: A multi-criteria approach. Int. J. Appl. Earth Obs. Geoinf. 101, 102347. https://doi.org/10.1016/j.jag.2021.102347.

Ishii, T., Simo-Serra, E., Iizuka, S., Mochizuki, Y., Sugimoto, A., Ishikawa, H., Nakamura, R., 2016. Detection by classification of buildings in multispectral satellite imagery. In: 23rd International Conference on Pattern Recognition (ICPR), Cancun, Mexico, pp. 3344–3349.

Justice, C.O., Giglio, L., Korontzi, S., Owens, J., Morisette, J.T., Roy, D., Descloitres, J., Alleaume, S., Petitcolin, F., Kaufman, Y., 2002. The MODIS fire products. Remote Sens. Environ. 83 (1-2), 244–262.

Kaufman, Y.J., Justice, C.O., Flynn, L.P., Kendall, J.D., Prins, E.M., Giglio, L., Ward, D.E., Menzel, W.P., Setzer, A.W., 1998. Potential global fire monitoring from EOS-MODIS. J. Geophys. Res.: Atm. 103 (D24), 32215–32238.

Kumar, S.S., Roy, D.P., 2018. Global operational land imager Landsat-8 reflectance-based active fire detection algorithm. Int. J. Digital Earth 11 (2), 154–178.

Leblon, B., 2001. Forest wildfire hazard monitoring using remote sensing: A review. Remote Sens. Reviews 20 (1), 1–43.

Lee, T.F., Tag, P.M., 1990. Improved detection of hotspots using the AVHRR 3.7-μm channel. Bull. Am. Meteorol. Soc. 71, 1722–1730.

Lee, C.M., Cable, M.L., Hook, S.J., Green, R.O., Ustin, S.L., Mandl, D.J., Middleton, E.M., 2015. An introduction to the NASA Hyperspectral InfraRed Imager (HyspIRI) mission and preparatory activities. Remote Sens. Environ. 167, 6–19.

Lorenz, E., 2013. Thermal Remote Sensing with Small Satellites: BIRD, TET and the Next Generation BIROS. In: Kuenzer, C., Dech, S. (Eds.), Thermal Infrared Remote Sensing: Sensors, Methods, Applications. Springer, Dordrecht, pp. 149–176.

Ma, L., Liu, Y.u., Zhang, X., Ye, Y., Yin, G., Johnson, B.A., 2019. Deep learning in remote sensing applications: A meta-analysis and review. ISPRS J. Photogramm. Remote Sens. 152, 166–177.

Marchese, F., Genzano, N., Neri, M., Falconieri, A., Mazzeo, G., Pergola, N., 2019. A Multi-Channel Algorithm for Mapping Volcanic Thermal Anomalies by Means of Sentinel-2 MSI and Landsat-8 OLI Data. Remote Sens. 11 (23), 2876. https://doi.org/ 10.3390/rs11232876.

Matsunaga, T., Iwasaki, A., Tsuchida, S., Iwao, K., Tanii, J., Kashimura, O., Nakamura, R., Yamamoto, H., Kato, S., Obata, K., Mouri, K., Tachikawa, T., 2019. HISUI status toward 2020 launch. In: IEEE IGARSS 2019, Yokohama, Japan, doi: 10.1109/ IGARSS.2019.8899179.

Morisette, J.T., Giglio, L., Csiszar, I., Justice, C.O., 2005. Validation of the MODIS active fire product over Southern Africa with ASTER data. Int. J. Remote Sense. 26 (19), 4239–4264.

Mueller, S.E., Thode, A.E., Margolis, E.Q., Yocom, L.L., Young, J.D., Iniguez, J.M., 2020. Climate relationships with increasing wildfire in the southwestern US from 1984 to 2015. Forest Ecol. Manag. 460, 117861. https://doi.org/10.1016/j. foreco.2019.117861.

Murphy, S.W., de Souza Filho, C.R., Wright, R., Sabatino, G., Correa Pabon, R., 2016. HOTMAP: Global hot target detection at moderate spatial resolution. Remote Sens. Environ. 177, 78–88.

Naitoh, M., Katayama, H., Harada, M., Nakamura, R., Kato, E., Tange, Y., Sato, R., Nakau, K., 2013. Compact Infrared Camera (CIRC) for Earth observation. In: The 29th Int. Sym. Sp. Tech. Sci. (ISTS), Nagoya, Japan, 6p.

Nieke, J., Rast, M., 2019 Status: Copernicus Hyperspectral Imaging Mission For The Environment (CHIME). In: IEEE IGARSS 2019, Yokohama, Japan, doi: 10.1109/ IGARSS.2019.8899807.

Roberts, G.J., Wooster, M.J., 2008. Fire Detection and Fire Characterization Over Africa Using Meteosat SEVIRI. IEEE Trans. Geosci. Remote Sens. 46 (4), 1200–1218.

Schroeder, W., Oliva, P., Giglio, L., Csiszar, I.A., 2014. The New VIIRS 375 m active fire detection data product: Algorithm description and initial assessment. Remote Sens. Environ. 143, 85–96.

Schroeder, W., Oliva, P., Giglio, L., Quayle, B., Lorenz, E., Morelli, F., 2016. Active fire detection using Landsat-8/OLI data. Remote Sens. Environ. 185, 210–220.

Sofan, P., Bruce, D., Jones, E., Marsden, J., 2019. Detection and validation of tropical peatland flaming and smouldering using Landsat-8 SWIR and TIRS bands. Remote Sens. 11 (4), 465. https://doi.org/10.3390/rs11040465.

Silvestri, M., Romaniello, V., Hook, S., Musacchio, M., Teggi, S., Buongiorno, M.F., 2020. First Comparisons of Surface Temperature Estimations between ECOSTRESS, ASTER and Landsat 8 over Italian Volcanic and Geothermal Areas. Remote Sens. 12, 184. https://doi.org/10.3390/rs12010184.

Urai, M., 2011. Volcano observations with aster and ASTER Image Database for Volcanoes. In: IEEE IGARSS 2011, Vancouver, BC, Canada, doi: 10.1109/ IGARSS.2011.6050018.

Williams, A.P., Abatzoglou, J.T., Gershunov, A., Guzman-Morales, J., Bishop, D.A., Balch, J.K., Lettenmaier, D.P., 2019. Observed impacts of anthropogenic climate change on wildfire in California. Earth's Future 7 (8), 892–910.

Wooster, M.J., Roberts, G., Perry, G.L.W., Kaufmann, Y.J., 2005. Retrieval of biomass combustion rates and totals from fire radiative power observations: FRP derivation and calibration relationship between biomass consumption and fire radiative energy release. J. Geophys. Res. 110 (D24311) https://doi.org/10.1029/2005JD006318.

Wooster, M.J., Roberts, G., Smith, A.M.S., Johnston, J., Freeborn, P., Amici, S., Hudak, A., 2013. Thermal Remote Sensing of Active Vegetation Fires and biomass burning events. In: Kuenzer, C., Dech, S. (Eds.), Thermal Infrared Remote Sensing: Sensors, Methods, Applications. Springer, Dordrecht, pp. 347–390.

Wright, R., Flynn, L., Garbeil, H., Harris, A., Pilger, E., 2002. Automated volcanic eruption detection using MODIS. Remote Sens. 82 (1), 135–155.

Wright, R., Flynn, L.P., Garbeil, H., Harris, A.J.L., Pilger, E., 2004. MODVOLC: near-real-time thermal monitoring of global volcanism. J. Volcanol. Geotherm. Res. 135 (1-2), 29–49.

Wright, R., 2016. MODVOLC: 14 years of autonomous observations of effusive volcanism from space. Geol. Society, London, Special Publ. 426 (1), 23–53.

Xu, Y., Xie, Z., Feng, Y., Chen, Z., 2018. Road extraction from high-resolution remote sensing imagery using deep learning. Remote Sens. 10, 1461. https://doi.org/ 10.3390/rs10091461.

Xu, W., Wooster, M.J., He, J., Zhang, T., 2020. First study of Sentinel-3 SLSTR active fire detection and FRP retrieval: Night-time algorithm enhancements and global intercomparison to MODIS and VIIRS AF products. Remote Sens. Environ. 248, 111947. https://doi.org/10.1016/j.rse.2020.111947.

Yamaguchi, Y., Kahle, A.B., Tsu, H., Kawakami, T., Pniel, M., 1998. Overview of Advanced Spaceborne Thermal Emission and Reflection Radiometer (ASTER). IEEE Trans. Geosci. Remote Sens. 36 (4), 1062–1071.

Zhang, T., Wooster, M.J., Xu, W., 2017. Approaches for synergistically exploiting VIIRS I-and M-Band data in regional active fire detection and FRP assessment: A demonstration with respect to agricultural residue burning in Eastern China. Remote Sens. Environ. 198, 407–424.